Highly Efficient and Selective Light-Driven Dry Reforming of Methane by a Carbon Exchange Mechanism

Hailong Xiong,[||] Yueyue Dong,[||] Canyu Hu, Yihong Chen, Hengjie Liu, Ran Long,* Tingting Kong,* and Yujie Xiong*
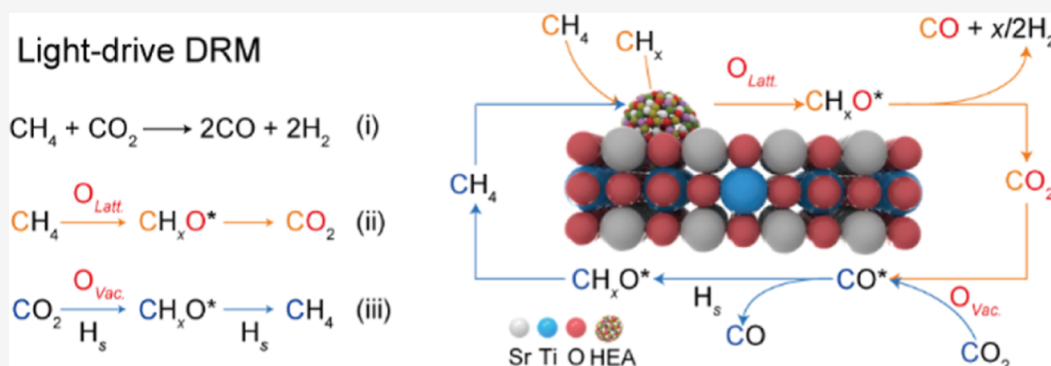
Cite This: *J. Am. Chem. Soc.* 2024, 146, 9465−9475

Read Online

ACCESS | Metrics & More | Article Recommendations | Supporting Information

ABSTRACT: Dry reforming of methane (DRM) is a promising technique for converting greenhouse gases (namely, CH_4 and CO_2) into syngas. However, traditional thermocatalytic processes require high temperatures and suffer from low selectivity and coke-induced instability. Here, we report high-entropy alloys loaded on $SrTiO_3$ as highly efficient and coke-resistant catalysts for light-driven DRM without a secondary source of heating. This process involves carbon exchange between reactants (i.e., CO_2 and CH_4) and oxygen exchange between CO_2 and the lattice oxygen of supports, during which CO and H_2 are gradually produced and released. Such a mechanism deeply suppresses the undesired side reactions such as reverse water−gas shift reaction and methane deep dissociation. Impressively, the optimized $CoNiRuRhPd/SrTiO_3$ catalyst achieves ultrahigh activity (15.6/16.0 mol g_{metal}^{-1} h^{-1} for H_2/CO production), long-term stability (∼150 h), and remarkable selectivity (∼0.96). This work opens a new avenue for future energy-efficient industrial applications.

INTRODUCTION

Methane (CH_4), the primary component in combustible ice, shale gas, and natural gas, is expected to be a sensible alternative to petroleum, yet its practical use in the petrochemical industry is precluded by the lack of cost-effective methods that can convert methane into valuable chemical feedstock.[1,2] Although dry reforming of methane (DRM; $CH_4 + CO_2 \rightarrow 2CO + 2H_2$) provides a feasible route to converting two major greenhouse gases (namely, CH_4 and CO_2) into syngas (i.e., CO and H_2), high reaction temperatures (700−1000 °C) are required to achieve sufficient yield owing to the thermodynamic constraints ($\Delta H_r = 247$ kJ mol^{-1}, $\Delta G_{298K} = 171$ kJ mol^{-1}), which inevitably increases fuel costs and leads to sintering and/or coking of catalysts ($CH_4 \rightarrow C + 2H_2$) (Figure 1a).[3,4] Moreover, the reverse water−gas shift (RWGS: $CO_2 + H_2 \rightarrow CO + H_2O$) side reaction is thermodynamically unavoidable, resulting in low selectivity referred to as the H_2/CO ratio.[5]

Recently, light-driven DRM has emerged as an environmentally friendly alternative for syngas production with economized energy consumption and eased catalyst deactivation.[1,6−8] In principle, a typical light-driven DRM process works with photogenerated charges or local heat (namely, photocatalysis or photothermal catalysis). In photocatalysis, CH_4 and CO_2 molecules are activated by photogenerated holes and electrons, respectively, on semiconductors (e.g., $SrTiO_3$, TiO_2, and CeO_2).[9−11] Despite the improved selectivity and stability, the activity is relatively low, owing to the kinetic limitation of multiple electron and hole transfer processes. In photothermal catalysis, reactants are activated by photogenerated local heat with a working mechanism similar to that of thermally driven DRM. The 3d transition metals (e.g., Ru, Rh, Pt, and Ni) supported on metal oxides rich in oxygen
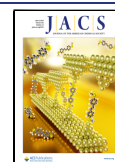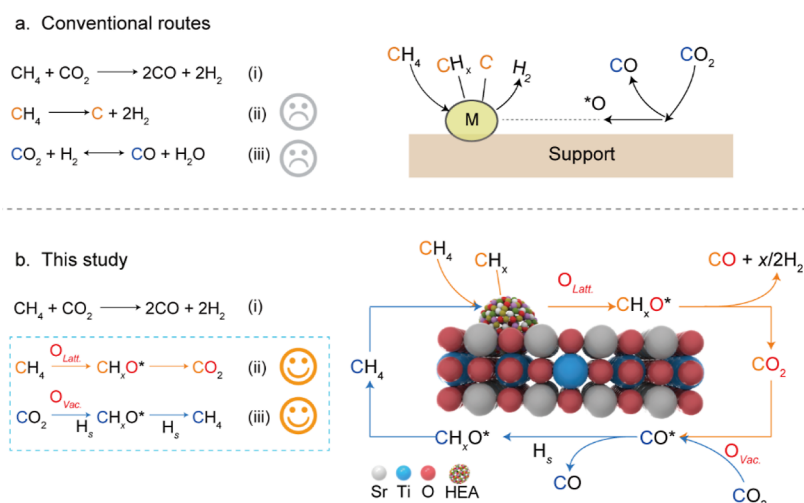
Figure 1. Schematic illustration of the proposed processes of DRM. (a) Conventional routes and (b) proposed reaction path, which involves the carbon exchange between reactants (i.e., CO_2 and CH_4) and the oxygen exchange between CO_2 and the lattice oxygen of supports. The yellow arrow represents the CH_4 to CO_2 conversion. The blue arrow represents the CO_2 to CH_4 conversion. M denotes 3d transition metals (e.g., Ru, Rh, Pt, or Ni). Supports denote metal oxides (e.g., CeO_2, MgO, or La_2O_3). HEA denotes the high-entropy alloy with the composition of CoNiRuRhPd. $O_{Latt.}$ and $O_{Vac.}$ denote the lattice oxygen and oxygen vacancy in $SrTiO_3$, respectively. H_s denotes the adsorbed hydrogen atom.

vacancies such as CeO_2 or alkaline oxide supports (e.g., MgO and La_2O_3) have been used as catalysts, which require input light intensity commonly exceeding 20 W cm^{-2} to reach the temperature of ~700 °C.[5,12−15] Although high light-to-fuel efficiency and catalytic activity can be achieved in such an approach, the stability and selectivity are compromised by the thermodynamically sustained RWGS reaction and coke deposition.[16] In this context, it remains a grand challenge to achieve high syngas yield and stability simultaneously in light-driven DRM under mild conditions. To this end, it is imperative to rationally design effective catalysts that can offer efficient C−H and C=O bond activation under mild conditions while restraining the undesired RWGS and catalyst deactivation.

In this regard, high-entropy alloys (HEAs), which contain five or more 3d transition metals (e.g., Co, Ni, Cu, Ru, Rh, Pd, and Pt) in a single solid solution phase, have been proven to exhibit excellent capability for C−H dissociation in propane dehydrogenation.[17] Moreover, the incompletely filled d states of components enable the HEAs to harvest photons throughout the entire solar spectrum via interband excitations, thereby offering superior photothermal conversion efficiency.[18,19] Undoubtedly, alkaline oxides can provide catalytically active sites for CO_2 adsorption and activation, particularly in the presence of oxygen vacancies.[20,21] As such, the combination of a HEA and alkaline oxide semiconductor would be a promising choice for opening up new opportunities in light-driven DRM, which may achieve high activity, selectivity, and stability under mild conditions by maneuvering reaction pathways.

Herein, we design HEAs on $SrTiO_3$ as a highly efficient and coke-resistant catalyst for light-driven DRM without a secondary source of heating, involving a new carbon exchange process (Figure 1b). In our design, Ni, Rh, Pd, and Ru are explored as the main active metals for CH_4 activation given their previously demonstrated potential for C−H cleavage.[15,22,23] $SrTiO_3$ with moderate alkaline sites is screened as the support to facilitate CO_2 adsorption and activation.[9,24,25] HEAs also absorb light in a wide spectrum and act as a

"nanoheater" to rapidly elevate the local temperature of the catalyst. Under 4 W cm^{-2} light irradiation, ultrahigh activity (15.6/16.0 mol g$_{metal}^{-1}$ h^{-1} for H_2/CO production), long-term stability (~150 h), and remarkable selectivity (~0.96) are achieved over CoNiRuRhPd loaded on $SrTiO_3$ (denoted as HEA/$SrTiO_3$). Similar catalytic performance can be obtained by using concentrated sunlight as the light source. Notably, the catalyst also exhibits superior performance in the dry reforming of ethane and propane, demonstrating the excellent universality of applications. In situ/quasi-in situ characterizations reveal that such outstanding performance is enabled by a new reaction path on the rationally designed catalyst, which involves the carbon exchange between reactants (i.e., CO_2 and CH_4) and the oxygen exchange between CO_2 and the lattice oxygen of the support. Due to the superior oxygen-releasing ability of HEA/$SrTiO_3$, CH_x ($0 \leq x \leq 3$) species from CH_4 activation on CoNiRuRhPd preferentially interact with lattice oxygen on $SrTiO_3$ to generate CH_xO^* species, which are further decomposed to syngas and even deeply oxidized to CO_2, leaving abundant oxygen vacancies on the catalyst surface. Meanwhile, apart from direct desorption yielding gaseous CO, the CO* species from CO_2 activation on $SrTiO_3$ also undergo hydrogenation to CH_4. The carbon exchange process inhibits the undesired side reactions such as the RWGS reaction and thus improves the selectivity to near unity as well as the atomic economic efficiency. Moreover, the oxygen vacancies left from CH_4 activation can be replenished by the O* species dissociated from CO_2 to run an oxygen cycle. Such a strategy guarantees the efficient transformation of CH_x^* to CH_xO^* intermediates and thus suppresses carbon deposits to enhance the long-term stability of the catalyst.

EXPERIMENTAL SECTION

Synthesis of Porous $SrTiO_3$. Porous $SrTiO_3$ was synthesized using a mild hydrothermal reaction.[26] In a typical synthesis, 25 mL of 1 M acetic acid solution containing 1.2 g of Sr(OH)$_2$·8H$_2$O and 10 mL of absolute ethanol containing 0.5 mL of TiCl$_4$ were mixed, followed by the addition of 2.5 g of NaOH. After stirring for 1 h at room temperature, the obtained mixture was transferred into a 50 mL Teflon-lined autoclave and heated at 200 °C for 48 h. After the
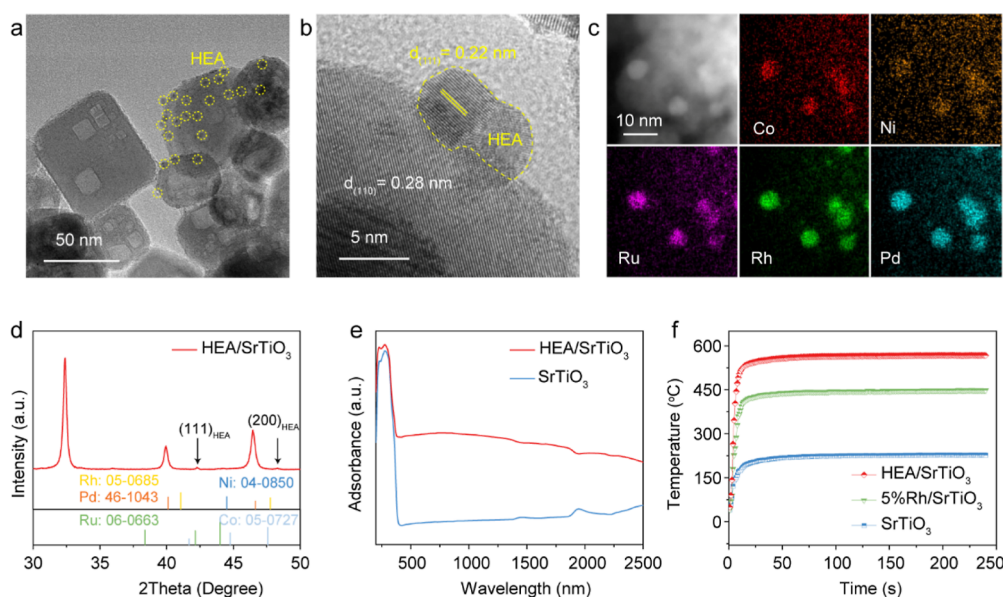
Figure 2. Morphology and structure characterization of the HEA/SrTiO$_3$catalyst. (a) TEM image, (b) HRTEM image, (c) HAADF-STEM images and EDS elemental mapping of Co, Ni, Ru, Rh, and Pd, and (d) XRD pattern of the HEA/SrTiO$_3$ catalyst. The standard data for Co (JCPDS no. 05-0727), Ni (JCPDS no. 04-0850), Ru (JCPDS no. 06-0663), Rh (JCPDS no. 05-0685), and Pd (JCPDS no. 46-0663) are presented at the bottom as references. (e) Diffuse reflectance UV−vis−NIR absorption spectra of SrTiO$_3$ and HEA/SrTiO$_3$ catalysts. (f) Surface local temperature evolution of SrTiO$_3$, 5% Rh/SrTiO$_3$, and HEA/SrTiO$_3$ catalysts under ~4 W cm^{-2} light irradiation.

hydrothermal process, the obtained products were separated by centrifugation (5000 rpm for 5 min) and thoroughly washed with distilled and anhydrous ethanol several times, followed by drying in air at 80 °C overnight.

Synthesis of HEA/SrTiO$_3$ Catalysts. Porous SrTiO$_3$ (230 mg) was added into 20 mL of deionized water under vigorous stirring for 0.5 h, followed by the addition of 1 mL of 10 mM solution for each metal precursor. After stirring for 1 h at room temperature, the obtained mixture was volatilized at 100 °C overnight to completely remove deionized water. Then, the resultant sample was calcined at 400 °C for 2 h (ramp rate 5 °C min^{-1}) in a 10% H$_2$/90% Ar atmosphere to yield CoNiCuRhPd/SrTiO$_3$, CoNiRuRhPd/SrTiO$_3$, PtNiRuRhPd/SrTiO$_3$, and AuNiRuRhPd/SrTiO$_3$. The loading of each metal on the SrTiO$_3$ was 1.0 mol %. Other CoNiRuRhPd-supported metal oxide catalysts with the same metal loadings were also prepared by using metal oxides instead of SrTiO$_3$ as the support materials. The single metal-loaded SrTiO$_3$ catalysts were synthesized in a similar way, except that the loading amount was changed to 5 mol %.

DRM Performance Measurements. DRM performance measurements were carried out under ambient pressure in a flow reactor (Beijing Scistar Technology Co., Ltd.) with a quartz window at the top for light irradiation. For each test, 5.0 mg of catalyst was uniformly dispersed on a glass fiber substrate with a diameter of 3 cm. The thickness of the catalyst layer was approximately 1 mm. After sealing the reactor, the reaction gas (10% CH$_4$/10% CO$_2$/80% Ar) was continuously introduced into the reactor with a flow rate of 20 mL min^{-1}. A 300 W xenon lamp (PLS-SXE300, Perfect light) was employed as the light source to drive the DRM reaction. After the equilibrium adsorption of feeding gas, the products were evaluated by an online gas chromatograph (GC-2014ATFSPL, Ar carrier, Shimadzu) equipped with two flame ionization detectors (FIDs) and a thermal conductivity detector (TCD). The dry reforming of C$_2$H$_6$ and C$_3$H$_8$ performance measurements were carried out in a similar process using 5% C$_2$H$_6$/10% CO$_2$/85% Ar flow and 3.33% C$_3$H$_8$/10% CO$_2$/86.67% Ar flow.

■ RESULTS AND DISCUSSION

Structural Characterizations. The porous SrTiO$_3$ sample was synthesized using a solvothermal coprecipitation reaction under relatively mild conditions.[26] Detailed results are shown in Figure S1. After the metal precursors were impregnated onto the SrTiO$_3$ surface, the H$_2$ temperature-programmed reduction (H$_2$-TPR) profiles show that the addition of a single metal generates broad reduction peaks at different temperatures (Figure S2). In comparison, a single reduction peak at ~140 °C—a temperature lower than that of the monocomponent counterpart—is induced by the quinary-component metal precursors of Co, Ni, Ru, Rh, and Pd. The simultaneous reduction of the metal precursors indicates that all atoms undergo interactions with each other, resulting in the formation of a solid solution alloy involving all five elements.[27] TEM and high-angle annular dark field scanning transmission electron microscopy (HAADF-STEM) images clearly show that the HEA nanoparticles (NPs), with an average diameter of ~2.0 nm, are evenly dispersed on the SrTiO$_3$ surface (Figures 2a and S3). A distinct lattice fringe spacing of 0.22 nm is observed in the high-resolution TEM (HRTEM) image, which can be attributed to the (111) plane of the face-centered cubic (fcc) phase of the HEA (Figures 2b and S4).[28] Energy-dispersive X-ray spectroscopy (EDS) mapping and line-scan data of the HEA/SrTiO$_3$ catalyst reveal the uniform distribution of Co, Ni, Ru, Rh, and Pd elements in individual particles without element segregation (Figures 2c and S5). Compared with bare SrTiO$_3$, the appearance of new diffraction peaks at 42.2 and 48.9° in the XRD pattern of the HEA/SrTiO$_3$ catalyst further suggests the formation of a single phase with the fcc structure,[27] whose lattice constant is intermediate between 3.5 Å for fcc Ni and 3.9 Å for fcc Pd (Figure 2d). No peaks attributed to pure Co, Ni, Ru, Rh, or Pd are detected. Taken together, the results above fully demonstrate the formation of a HEA on SrTiO$_3$.

X-ray absorption fine structure (XAFS) spectroscopy was further conducted to acquire structural information on the samples. Figure S6a1−c1 shows the K-edge X-ray absorption near-edge structure (XANES) spectra of Co, Ni, and Pd in the
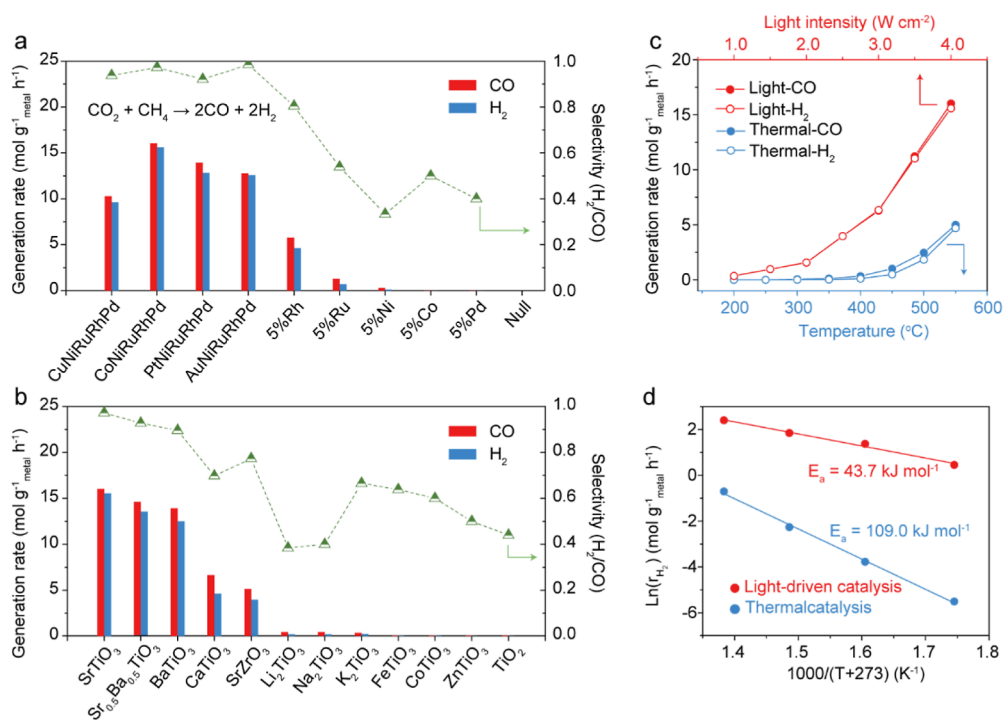
Figure 3. Light-driven DRM performance. Yields of H_2 and CO by (a) mono- and quinary-component metal-loaded $SrTiO_3$ catalysts and (b) HEA-loaded catalysts. Reaction conditions: feeding gas of 10% CO_2/10% CH_4/80% Ar, total space velocity of 20 mL min^{-1}, 5 mg of catalyst, 300 W Xe lamp with a light intensity of 4.0 W cm^{-2}. (c) Yields of H_2 and CO by the HEA/SrTiO$_3$ catalyst under light irradiation and external heating with the temperature equal to that of the photothermal temperature. (d) Arrhenius plots for H_2 production rates of the HEA/SrTiO$_3$ catalyst under light-driven and thermal-driven conditions.

HEA, respectively. The postedges of Co, Ni, and Pd elements show slight deviations in intensity, shape, and oscillation behavior compared with metal foils, indicating the redistribution of electrons among the three elements and the unique orbital hybridizations.[29] The extended XAFS (EXAFS) spectra (Figure S6a2−c2) reveal the overlapping of the characteristic peaks of three elements and the distance of all the first metal− metal (M−M) shells is obviously shorter than that of the corresponding metal foils, indicating the existence of atomic interactions between the constituent elements.[28]

The light-harvesting ability of the HEA/SrTiO$_3$ catalyst was characterized by diffuse reflectance ultraviolet−visible−near-infrared (UV−vis−NIR) absorption spectroscopy. Compared with bare SrTiO$_3$, the loading of the HEA greatly extends the light absorption from the UV region to the broadband UV−vis−NIR region (200−2500 nm) (Figure 2e), which enables the HEA/SrTiO$_3$ catalyst to function as a good "nanoheater". On this basis, the photothermal conversion property of such a material was further tested using a thermocouple in close contact with the catalyst surface under different light intensities. When the light intensity is 4.0 W cm^{-2}, the temperature of the HEA/SrTiO$_3$ catalyst bed reaches 560 °C, substantially higher than those of the single metal-loaded catalyst (i.e., Rh/SrTiO$_3$) (448 °C) and bare SrTiO$_3$ (227 °C) (Figure 2f). The result indicates that HEA/SrTiO$_3$ can potentially serve as an efficient light-harvesting platform to drive DRM under mild conditions.

Light-Driven DRM Performance. The DRM performance of the as-prepared catalysts was evaluated using a flow reactor apparatus under 300 W Xe lamp irradiation without a secondary source of heating. The space velocity and reaction gas concentration were first optimized to be 20 mL min^{-1} and

10% CH_4/10% CO_2/80% Ar, respectively (Figure S7 and Table S1). Furthermore, catalysts with various metal species supported on SrTiO$_3$ were investigated. As shown in Figures 3a and S8a, bare SrTiO$_3$ shows negligible activity. After loading single metals, only Ni-, Rh-, and Ru-supported catalysts can drive DRM (see also Table S2), indicating certain ability of these metals in C−H bond dissociation. Interestingly, upon the introduction of HEAs (MNiRuRhPd, where M = Cu, Co, Pt, or Au), the catalytic performance is dramatically enhanced, most likely attributed to the ensemble effect of HEAs. Among the catalysts, the composition of CoNiRuRhPd (denoted as HEA) exhibits the highest catalytic activity for DRM.

Upon ascertaining the HEA, various catalyst supports such as MTiO$_3$ (M = Ba, Ca, Li, Na, K, Fe, Co, Zn, etc.) were subsequently examined. Among the supports, Sr$_x$Ba$_{1−x}$TiO$_3$, CaTiO$_3$, and SrZrO$_3$ are manifested to be the appropriate supports due to their similar physical and chemical properties with activity in the following order: SrTiO$_3$ > Sr$_{0.5}$Ba$_{0.5}$TiO$_3$ > BaTiO$_3$ > CaTiO$_3$ > SrZrO$_3$ (Figures 3b, S9−S12 and Table S3). In sharp contrast, TiO$_2$ and other MTiO$_3$ (M = Li, Na, K, Fe, Co, or Zn) are not conductive supports for DRM (Figure S8b). The yields of syngas over these supported HEA catalysts are 700 times lower than that of HEA/SrTiO$_3$, and the selectivity referred to as the ratio of H_2 to CO by these catalysts is generally lower than 0.8. The superior activity of HEA/SrTiO$_3$ may be attributed to the presence of moderate basic sites in SrTiO$_3$ support, which are helpful for the adsorption and activizaton of CO_2 (Figures S13 and S14, and Table S4).[30]

To summarize, in consideration of catalytic efficiency and selectivity, we find that the highest overall DRM performance is provided by the composition of CoNiRuRhPd/SrTiO$_3$ (i.e.,
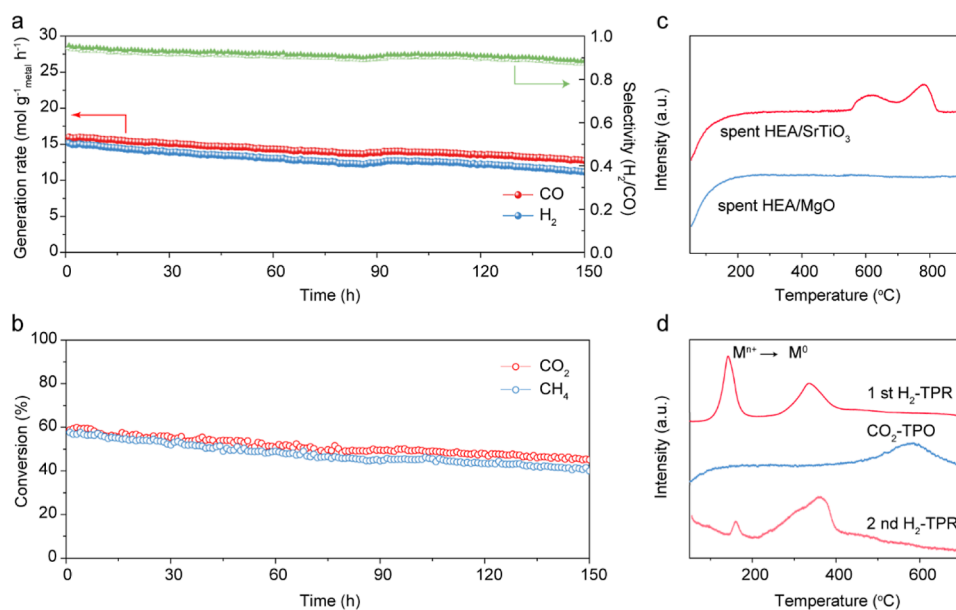
Figure 4. Long-term stability of the HEA/SrTiO$_3$catalyst. Time course of the (a) selectivity and yield of H$_2$ and CO and (b) conversion of CH$_4$ and CO$_2$. Reaction conditions: feeding gas of 10% CO$_2$/10% CH$_4$/80% Ar, total space velocity of 20 mL min^{-1}, 5 mg of catalyst, 300 W Xe lamp with a light intensity of 4.0 W cm^{-2}. (c) CO$_2$ TPSR for HEA/SrTiO$_3$ used in DRM for 150 h and HEA/MgO used in DRM for 40 h. (d) CO$_2$-titration (TPO) experiment for the oxygen vacancies of SrTiO$_3$ using HEA/SrTiO$_3$.

HEA/SrTiO$_3$). The single-pass conversion of CH$_4$ and CO$_2$ over HEA/SrTiO$_3$ reaches 56.2 and 58.6%, respectively, and the evolution rates of H$_2$ and CO normalized by the mass of the HEA are as high as 15.6 and 16.0 mol g$_{metal}^{-1}$ h^{-1}, respectively (Figure 3a,b). Moreover, the light-to-fuel efficiency of HEA/SrTiO$_3$ can be calculated to be approximately 2.1%. Notably, the selectivity in yield is up to 0.96, and byproducts such as oxygenates and hydrocarbons are not observed, suggesting that the products can be directly used in the Fischer–Tropsch synthesis without extra steps of adjusting selectivity via a high-temperature water–gas shift reaction (CO + H$_2$O → H$_2$ + CO$_2$). This excellent performance significantly exceeds the benchmark state-of-the-art reports, including low-temperature thermocatalysis, photocatalysis, photo-assisted thermocatalysis, and photothermal catalysis (Figure S15 and Table S5). In addition to DRM, the HEA/SrTiO$_3$ catalyst can also catalyze the dry reforming of ethane (C$_2$H$_6$) and propane (C$_3$H$_8$) with high activity and selectivity (Figures S16 and S17), confirming the general applicability of the as-prepared catalyst.

For practical applications, solar-driven DRM was performed on a typical sunny day (16 October 2022) at the University of Science and Technology of China in Hefei (31.52 N, 117.17 E). By using a Fresnel lens with a diameter of 20 cm to concentrate sunlight to approximately 40 suns, evolution rates of H$_2$ at 15.0 mol g$_{metal}^{-1}$ h^{-1} and CO at 15.4 mol g$_{metal}^{-1}$ h^{-1} were achieved, very close to those obtained by xenon lamp irradiation (Figure S18). This result indicates that an artificial light source can be used to drive the DRM reaction at night or during inclement weather, while concentrated natural sunlight can drive this reaction in other time periods, resulting in sustainable production of solar fuel.

Light intensity- and temperature-dependent (the temperatures were set equal to that of photothermal temperatures) experiments were performed to clarify the specific roles of light on DRM. With the increase in the light intensity from 1.0, 2.0, and 3.0 to 4.0 W cm^{-2}, the photothermal temperature of HEA/SrTiO$_3$ gradually increases from 220, 300, and 450 to 560 °C (Figure S19). Under 4.0 W cm^{-2} of light irradiation, the catalytic activity is much higher than that of thermocatalysis at 560 °C in the dark (Figure 3c, and Table S6). As the light intensity is lowered to 2.0 or even 1.0 W cm^{-2}, the evolution rate of H$_2$ is still up to 1.57 and 0.35 mol g$_{metal}^{-1}$ h^{-1}, respectively. In stark contrast, no DRM occurs with external heating below 350 °C. In comparison to the theoretical equilibrium conversions, light-driven catalysis breaks through the theoretical limitation of DRM (Figure S20). These results indicate that the light-driven DRM is not merely a photothermal catalysis but likely involves photocatalysis.

To gain further insights into the role of light in DRM, an in situ irradiated X-ray photoelectron spectroscopy (XPS) characterization was performed. As shown in Figure S21, an apparent positive shift in the Ti 2p binding energy and a negative shift in the Rh 3d and Pd 3d binding energies of HEA/SrTiO$_3$ can be observed after 120 min of light irradiation. These indicate that the photoexcited energetic electrons generated from the conduction band of SrTiO$_3$ can transfer to the adjacent HEA NPs (see also Figure S22).[7,25] Therefore, it can be reasonably inferred that HEA NPs act as electron capture centers with high electron density, promoting the activation of CO$_2$ and thus enhancing the catalytic properties. Taken together, the light-driven DRM process over HEA/SrTiO$_3$ involves a synergy of photocatalysis and photothermal catalysis.[31] The apparent activation energies (E_a) of DRM over HEA/SrTiO$_3$ via the light-driven and thermocatalytic routes are calculated to be 43.7 and 109.0 kJ mol^{-1}, respectively, according to the Arrhenius plots (Figure 3d). The lower E_a under light-driven conditions indicates that light irradiation greatly reduces the activation energy barrier of the DRM.

In addition to catalytic activity and selectivity, stability is another limitation that our work aims to overcome. To this end, the long-term stability and reusability of HEA/SrTiO$_3$ were examined. Figure 4a,b shows that almost no noticeable
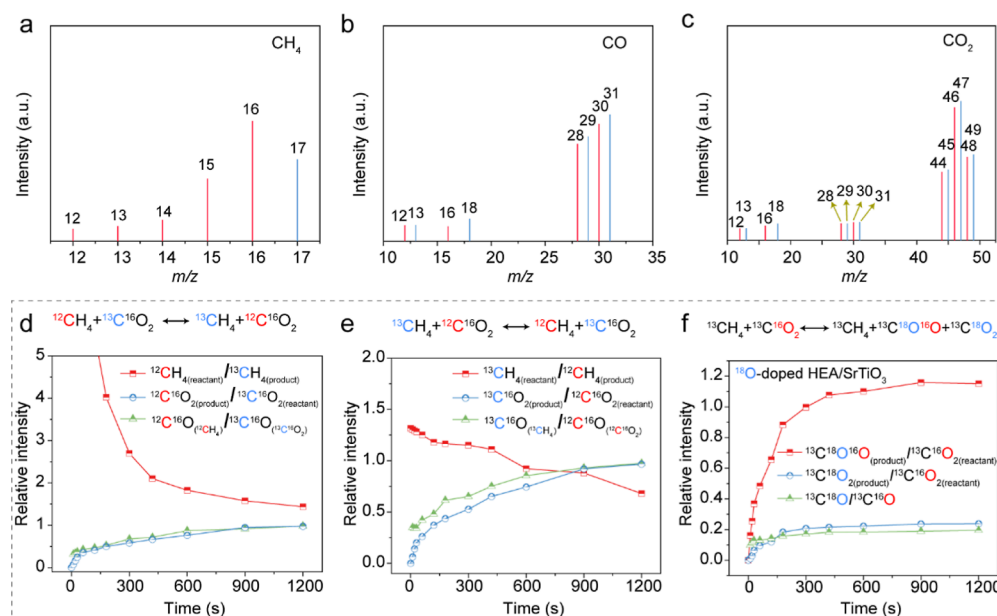
Figure 5. [13]C- and ^{18}O-labeled isotope-labeling experiments. Mass spectra of (a) CH_4, (b) CO, and (c) CO_2 over HEA/SrTiO$_3$ after 20 min of light irradiation using an equivalent amount of $^{13}CH_4$ and $^{12}C^{18}O_2$ as the feeding gas. Carbon exchange between CO_2 and CH_4 as a function of reaction time over HEA/SrTiO$_3$ using equivalent amounts of (d) $^{12}CH_4$ and $^{13}C^{16}O_2$ and (e) $^{13}CH_4$ and $^{12}C^{16}O_2$ as feeding gases. (f) Oxygen exchange between $^{13}C^{16}O_2$ and the lattice oxygen in SrTiO$_3$ as a function of reaction time over ^{18}O-doped SrTiO$_3$ using an equivalent amount of $^{13}CH_4$ and $^{13}C^{16}O_2$ as the feeding gas. Reaction conditions: 5 mg of catalyst and 300 W Xe lamp with a light intensity of 4.0 W cm^{-2}.

activity loss is detected after continuous operation for 40 h. The carbon balance and oxygen balance are close to unity, indicating a minor contribution of coking to the HEA/SrTiO$_3$ catalyst. Even after 150 h on stream, the catalytic activity decreases slightly with ~82% of the initially observed activity remaining. The morphology of the spent HEA/SrTiO$_3$ used in DRM for 150 h is almost unchanged without obvious aggregation of HEA NPs (Figure S23a,b). EDS mapping and line-scan data demonstrate the uniform distribution of five elements in individual particles, suggesting that the spent catalyst maintains a high-entropy structure (Figure S23c–e). Raman spectra (Figure S24) and the O$_2$ temperature-programmed oxidation (TPO) profiles (Figure S25) reveal that only a trace amount of carbon species is detected on the HEA/SrTiO$_3$ surface after 150 h of DRM, indicating the high coking resistance of the catalyst. In sharp contrast, although HEA/Al$_2$O$_3$ and HEA/MgO offer fair initial yields of syngas, severe deactivation occurs within 40 h, accompanied by low carbon and oxygen balance (Figure S26). Such performance decay accords with the observation of carbon deposition; a black substance is formed on the catalyst surface soon after light exposure and is ascertained as graphitic carbon by Raman spectroscopy (Figure S24). TEM images of HEA/Al$_2$O$_3$ and HEA/MgO after the reaction also confirm that carbon nanofibers are formed around the HEA NPs after DRM (Figure S27).

The observed stability difference strongly suggests the importance of the supports against coking. Temperature-programmed surface reactions (TPSRs) were conducted to examine the coking resistance of HEA/SrTiO$_3$. When exposed to CO$_2$ flow, the spent HEA/SrTiO$_3$ removes coke at 550–800 °C due to the continuous oxygen supply from CO$_2$, whereas the spent HEA/MgO cannot (Figure 4c). This indicates the superior CO$_2$ activation capacity of SrTiO$_3$, as further illustrated by the CH$_4$-TPSR and CO$_2$-TPSR measure-

ments (Figure S28).[32] In addition, we verified the filling of oxygen vacancies after the lattice oxygen consumption of SrTiO$_3$ using CO$_2$ titration via a TPO technique.[33] As shown in Figure 4d, the oxygen vacancies generated by H$_2$-TPR in SrTiO$_3$ can be filled by the oxygen atoms dissociated from CO$_2$ and then reappear after further H$_2$ reduction, indicating that SrTiO$_3$ has the ability to cyclically release oxygen. Based on the above results, we infer that the efficient activation of CO$_2$ and oxygen-releasing ability of HEA/SrTiO$_3$ are responsible for the coking resistance.

Reaction Mechanism. The information gleaned above recognized the superior performance of HEA/SrTiO$_3$. Naturally, a question arises as to what working mechanism is responsible for such giant progress. Isotope-labeling experiments were first performed to trace the origin of products. When using ^{13}C-labeled substances ($^{13}C^{16}O_2$ and $^{13}CH_4$) as the feeding gas, the peak located at 1.8 min with $m/z = 29$ in the mass spectrum can be assigned to ^{13}CO, indicating that the produced CO indeed originates from fed CO$_2$ and CH$_4$ (Figure S29). Surprisingly, when ^{18}O- and ^{13}C-labeled substances ($^{12}C^{18}O_2$ and $^{13}CH_4$) served as feeding gas, the mass spectrum of CH$_4$ shows that the intensity of $m/z = 16$ is obviously higher than that of $m/z = 17$ (Figure 5a). Moreover, four distinct m/z, namely,[28] ($^{12}C^{16}O$), 29 ($^{13}C^{16}O$), 30 ($^{12}C^{18}O$), and 31 ($^{13}C^{18}O$), were observed in the mass spectrum of CO (Figure 5b). Six distinct m/z values, namely, 44 ($^{12}C^{16}O_2$), 45 ($^{13}C^{16}O_2$), 46 ($^{12}C^{16}O^{18}O$), 47 ($^{13}C^{16}O^{18}O$), 48 ($^{12}C^{18}O_2$), and 49 ($^{13}C^{18}O_2$), were detected in the mass spectrum of CO$_2$ (Figure 5c). These results indicate the simultaneous occurrence of carbon exchange between $^{12}C^{18}O_2$ and $^{13}CH_4$ (i.e., carbon exchange) and oxygen exchange between $^{12}C^{18}O_2$ and the lattice oxygen of SrTiO$_3$ in DRM.

Previous studies have shown that the oxygen exchange between CO$_2$ and the lattice oxygen readily occurs via a Mars–van Krevelen-type mechanism using metal oxides (e.g., CeO$_2$
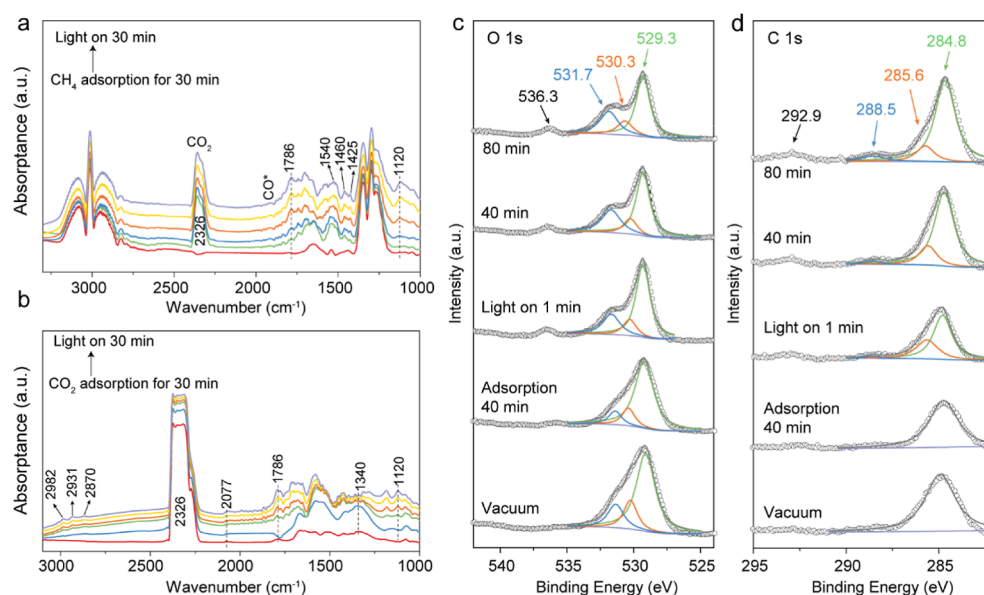
Figure 6. In situ characterization of light-driven DRM. In situ DRIFTS spectra for the adsorption and activation of CH_4 (a) and CO_2 (b) collected over the HEA/SrTiO$_3$ catalyst under light illumination. In situ NAP-XPS O 1s (c) and C 1s (d) spectra of HEA/SrTiO$_3$ collected under 0.5 mbar CO_2 and 0.5 mbar CH_4 atmospheres with different light illumination times.

and La$_2$O$_3$) as supports during the oxidation of CH$_x$* in DRM, which has been considered as an effective strategy to enhance the stability of catalysts.[9,15,34] It is worth mentioning that the carbon exchange between the reactants (i.e., CO_2 and CH_4) is an unusual phenomenon due to its kinetically unfavorable nature. To examine this process, quasi-in situ isotope-labeling experiments were carried out using $^{12}CH_4$ + $^{13}CO_2$ (system I) as the feeding gas. As shown in Figure S30, m/z = 44 ($^{12}CO_2$) and m/z = 17 ($^{13}CH_4$) appear and gradually increase along with the decrease in m/z = 45 ($^{13}CO_2$) and m/z = 16 ($^{12}CH_4$) under continuous light irradiation, confirming the occurrence of carbon exchange between CH_4 and CO_2 ($^{12}CH_4$ + $^{13}C^{16}O_2$ ↔ $^{13}CH_4$ + $^{12}C^{16}O_2$).

To quantitatively analyze the kinetics of carbon exchange, the intensity ratios of m/z = 44 (product $^{12}CO_2$) to m/z = 45 (reactant $^{13}CO_2$) (abbreviated as $^{12}CO_{2(product)}/^{13}CO_{2(reactant)}$) and m/z = 16 (reactant $^{12}CH_4$) to m/z = 17 (product $^{13}CH_4$) (abbreviated as $^{12}CH_{4(reactant)}/^{13}CH_{4(product)}$) were calculated (see Supporting Information for the calculation of reaction kinetics). As shown in Figure 5d, the value of $^{12}CO_{2(product)}/^{13}CO_{2(reactant)}$ gradually increases while the value of $^{12}CH_{4(reactant)}/^{13}CH_{4(product)}$ decreases and finally reaches equilibrium at 10 min. The value of $^{12}CO_{2(product)}/^{13}CO_{2(reactant)}$ is close to 1.0 at dynamic equilibrium, proving the sufficient exchange of the carbon element between CH_4 and CO_2. Similarly, the intensity ratio of m/z = 28 (^{12}CO from $^{12}CH_4$) to m/z = 29 (^{13}CO from $^{13}CO_2$) (abbreviated as $^{12}CO/^{13}CO$) is also close to 1.0, suggesting that half of the produced CO originates from $^{12}CH_4$ while the other half comes from $^{13}CO_2$. Notably, if side reactions such as the RWGS occur, the product CO would not only originate from DRM ($CH_4 + CO_2 \rightarrow 2CO + 2H_2$) but also come from a RWGS ($CO_2 + H_2 \rightarrow CO + H_2O$). Based on this assumption, the intensity ratio of CO from CH_4 to CO from CO_2 will be much less than 1.0. Therefore, it is reasonable to infer that almost no RWGS reaction occurs, leading to high selectivity (~0.96). A similar phenomenon can also be observed with system II ($^{13}CH_4$ and $^{12}C^{16}O_2$) as the feeding gas, as shown in

Figures 5e and S31. In sharp contrast, when HEA/Al$_2$O$_3$ and HEA/MgO are used as catalysts, no reversible carbon exchange occurs in DRM (Figures S32 and S33). The selectivities of the HEA/Al$_2$O$_3$ and HEA/MgO catalysts are 0.57 and 0.68, respectively (Table S5). Taken together, the occurrence of carbon exchange may be responsible for the selectivity of DRM.

The oxygen exchange process was studied by using ^{18}O-doped HEA/SrTiO$_3$ as a catalyst with system III ($^{13}CH_4$ and $^{13}C^{16}O_2$) as the feeding gas. Kinetic analysis reveals that the oxygen exchange between $^{13}C^{16}O_2$ and ^{18}O-doped SrTiO$_3$ occurs quickly and reaches dynamic equilibrium within 5 min (Figures 5f and S34). Coincidentally, an analogous phenomenon can also be observed when system IV ($^{12}CH_4$ and $^{12}C^{16}O_2$) was used as the feeding gas (Figure S35). These results fully confirm the superior ability of HEA/SrTiO$_3$ to release oxygen, in agreement with the CO$_2$-titration experiments (Figure 4d), which may facilitate long-term stability. More importantly, when HEA/BaTiO$_3$ was used as a catalyst instead of HEA/SrTiO$_3$, the phenomenon of carbon exchange and oxygen exchange can also be observed, suggesting its general applicability (Figure S36).

For the DRM reaction mechanism, the elementary steps of DRM generally involve the CO_2 dissociation to CO* and O*, the step-by-step CH_4 dissociations to CH$_x$* (x = 0−3) and H*, the interaction of CH$_x$* with O* or lattice oxygen of supports to CH$_x$O*, and the transformation of CH$_x$O* to CO.[31,35,36] To gain insights into the mechanism of carbon exchange between CO_2 and CH_4, in situ DRIFTS was employed to individually investigate CO_2/CH_4 adsorption and activation on HEA/SrTiO$_3$. The catalyst was first exposed to a 10% CH_4/90% Ar flow in the dark for adsorption. As shown in Figure S37, apart from the C−H deformation vibration of gaseous CH_4 (3002, 1340, 1302, and 1267 cm^{-1}), an additional C−H symmetric deformation vibrational mode of adsorbed CH_4 (1540 cm^{-1})[37,38] was observed on HEA/SrTiO$_3$. Upon light irradiation, the vibrational modes of CH$_2$/CH$_3$ deformation (1460 and 1425 cm^{-1})[37] and CH$_x$O*
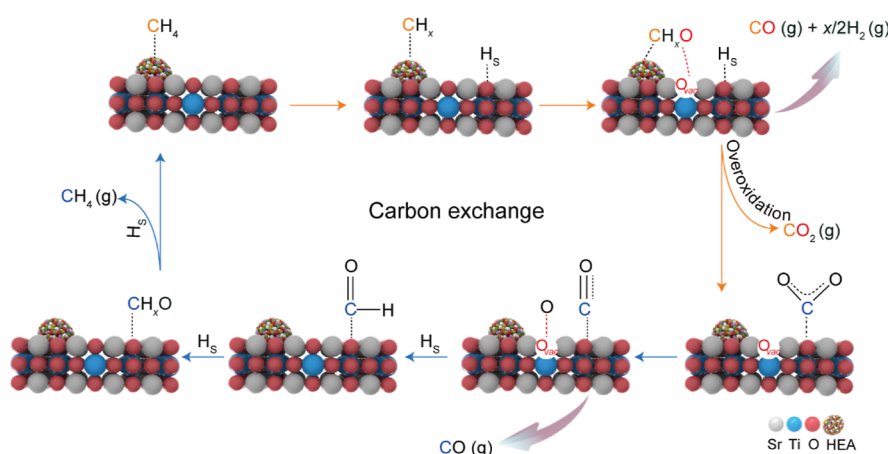
Figure 7. Reaction mechanism for light-driven DRM. Yellow and blue arrows indicate the carbon exchange between CH_4 and CO_2. Red dashes represent the oxygen exchange between CO_2 and the lattice oxygen of $SrTiO_3$. H_s denotes the hydrogen atom from the spillover.

species (1120 cm^{-1})[39−41] appear, while the C−H symmetric deformation vibration of CH_4 decreases gradually, indicating the dissociation of CH_4 to CH_x or CH_xO^* species (Figure 6a). Moreover, the strong peak at 2326 cm^{-1} attributed to gaseous CO_2 and the weak peaks at 2016−1876 cm^{-1} attributed to adsorbed CO^* appear,[39] indicating the oxidation of CH_4 to CO_2 and a small amount of CO, as further proven by the ^{13}C-labeled CH_4 conversion experiments (Figure S38). Naturally, there are two possible reaction paths leading to CH_4 to CO_2 conversion. The first is the step-by-step CH_x^* dehydrogenation to C and H_2 ($CH_4 \rightarrow C + 2H_2$) and the oxidization of C by the lattice oxygen of $SrTiO_3$ to CO and CO_2.[36] The second is the transformation of CH_xO^* intermediates to CO_2, CO, and H_2O.[42,43] The CH_4-TPD mass spectra (Figure S39) reveal that the CH_4 desorption products on $HEA/SrTiO_3$ are mainly CO_2 and H_2O as well as a small amount of CO. Note that no C or H_2 is detected. This result fully confirms that CH_4 adsorbed on the catalyst surface tends to be oxidized to CO_2 via the CH_xO^* intermediates, rather than being progressively dehydrogenated to C and H_2.[43] Therefore, it can be reasonably inferred that the CH_4 to CO_2 transformation pathway in DRM takes place as follows: CH_4 is dissociated to CH_x^* and H^* species, CH_x^* interacts with the lattice oxygen of supports to give CH_xO^*, and CH_xO^* transforms to CO_2 and CO (Figure S40a).

The in situ DRIFTS of CO_2 adsorption shows the linearly adsorbed CO^* (2077 cm^{-1}),[39] formyl species (HCO*, 1786 and 1340 cm^{-1}),[44,45] bicarbonates (1640, 1422 and 1080 cm^{-1}),[46,47] and formate species (1666, 1580, and 1393 cm^{-1})[48,49] (Figure S41). This indicates that CO_2 can be activated into the CO^* and the O^* species, in which the CO^* species further interact with the surface hydroxyl groups or hydrogen on the catalyst to form the HCO* species. Under light irradiation, additional peaks at 2870 cm^{-1} [$\nu(CH)$], 2931 cm^{-1} [$\nu(CH_3)$], and 1120 cm^{-1} (CH_xO^*)[39−41] appear and gradually grow along with the consumption of HCO* species (Figure 6b), indicating that the adsorbed CO^* species could be transformed into CH_xO^* intermediates by sequential hydrogenation.[50] In situ DRIFTS spectra for CO adsorption show that the bridge-adsorbed CO^* species at 1890 cm^{-1} on $HEA/SrTiO_3$ are relatively stable and not easy to desorb[39] (Figure S42), which allows for the adsorbed CO^* species to be hydrogenated into CH_4.[51,52] Accordingly, we infer the CO_2 to CH_4 transformation pathway in DRM as follows: CO_2

dissociation to CO^* and O^* species, and CO^* hydrogenation to CH_xO^* and then to CH_4 (Figure S40b).

In situ DRIFTS was further conducted under a DRM atmosphere. Under light irradiation, both linearly (2077 cm^{-1}) and bridged adsorbed CO (1866 cm^{-1}) appear immediately[39] (Figure S43). Furthermore, the appearance of CH_xO^* intermediates on $HEA/SrTiO_3$,[39,41] along with the first consumption and then increase in formyl species, clearly suggests that the CH_xO^* species are indeed the critical intermediates. We thus can conclude that the interaction between CO_2-dissociated species and CH_4-dissociated species leads to the reversible formation and decomposition of CH_xO^* species,[43] causing the element scrambling between CH_4 and CO_2. This carbon exchange process restricts the undesired RWGS reaction to some extent and thus improves the selectivity to near unity and the atomic economic efficiency.

For further consolidation, the surface-absorbed species were also analyzed by in situ near ambient pressure XPS (NAP-XPS) studies. The initial high-resolution O 1s XPS spectrum for $HEA/SrTiO_3$ collected in ultrahigh vacuum reveals three distinct peaks located at 529.3, 530.3, and 531.7 eV, which can be ascribed to the lattice oxygen, oxygen vacancy, and surface labile oxygen, respectively (Figure 6c).[53] After introducing 0.5 mbar CO_2 and 0.5 mbar CH_4 into the NAP-XPS chamber in the dark, the peaks of gas-phase CO_2 (292.9, 536.3 eV) are observed (Figure 6c,d).[54] Moreover, the peak intensity of oxygen vacancies greatly decreases, indicating that the oxygen vacancies on $SrTiO_3$ are the main active sites for CO_2 adsorption, as further confirmed by NAP-XPS collected under a 1.0 mbar CO_2 atmosphere (Figure S44). With light irradiation, the peaks of carboxyl species at 288.5 eV[55,56] and CH_xO^* intermediates at 285.6 eV gradually appear[57,58] (Figure 6d), in agreement with the DRIFTS results. Notably, the peak intensities for lattice oxygen of $SrTiO_3$ gradually decrease, suggesting that lattice oxygen may act as a mediator to facilitate the transformation of CH_x^* to CH_xO^* intermediates along with the regeneration of surface oxygen vacancies (see also Figure S45 and Table S7).[9,37,38] The continuous consumption and regeneration of oxygen vacancies and lattice oxygen lead to the oxygen exchange between CO_2 and the lattice oxygen of $SrTiO_3$, in agreement with the CO_2-titration experiments and the isotope-labeling experiments. According to the above results, CH_x^* species prefer to interact with lattice oxygen of $SrTiO_3$ to generate CH_xO^* inter-

mediates rather than direct dehydrogenation to C adsorbates, which may be responsible for the coke-resistant stability.[35]

According to the above results, we propose a new carbon exchange process of the light-driven DRM over HEA/SrTiO$_3$ in Figure 7. During DRM, CH$_4$ is adsorbed on the HEA surface and undergoes dissociation under light irradiation, forming CH$_x$* and H* species (Figure 7, yellow reaction path; see also Figure S40a), as confirmed by the in situ DRIFTS spectra (Figure 6a). The H* species migrate along the catalyst surface through spillover, providing a hydrogen source for further reactions. Due to the superior oxygen-releasing ability of HEA/SrTiO$_3$, CH$_x$ species preferentially interact with lattice oxygen on SrTiO$_3$ to generate CH$_x$O* species, which are further decomposed to syngas and even deeply oxidized to CO$_2$ (the CH$_4$ to CO$_2$ transformation pathway), leaving abundant oxygen vacancies on the catalyst surface, as proven by the in situ NAP-XPS spectra (Figure 6c). Meanwhile, CO$_2$ is preferentially adsorbed on the oxygen vacancies of SrTiO$_3$ and then dissociated into adsorbed CO* and O* species (Figure 7, blue reaction path; Figure S40b). Apart from direct desorption yielding gaseous CO, the adsorbed CO* species also undergo hydrogenation to CH$_4$ (the CO$_2$ to CH$_4$ transformation pathway), according to the in situ DRIFTS spectra (Figure 6b). This carbon exchange process restricts the undesired RWGS reaction to some extent and thus improves the selectivity to near unity and the atomic economic efficiency. The adsorbed O* species replenish oxygen vacancies left from CH$_4$ activation, regenerating lattice oxygen and providing the guarantee for the efficient transformation of CH$_x$* to CH$_x$O* intermediates, as confirmed by the in situ NAP-XPS spectra (Figure 6c). This oxygen exchange between CO$_2$ and the lattice oxygen of SrTiO$_3$ suppresses the step-by-step CH$_x$* dehydrogenation to carbon deposits and thus enhances the long-term stability.

CONCLUSIONS

In summary, we designed an HEA (CoNiRuRhPd) on SrTiO$_3$ as a highly effective catalyst for light-driven DRM. Benefiting from the excellent light absorption capacity and C−H dissociation ability of the HEA, DRM can be efficiently driven under light irradiation without a secondary source of heating. A new reaction path was proposed according to in situ/quasi-in situ characterizations. The reaction path involves carbon exchange between reactants (i.e., CO$_2$ and CH$_4$) and oxygen exchange between CO$_2$ and the lattice oxygen of supports via CH$_x$O intermediates, during which CO and H$_2$ are gradually produced and released. As a result, the HEA/SrTiO$_3$ catalyst achieves an ultrahigh syngas yield (evolution rates of H$_2$ and CO at 15.6 and 16.0 mol g$_{metal}^{-1}$ h^{-1}, respectively), outstanding selectivity (∼0.96), and long-term stability (with >82% initial activity maintained after 150 h of reaction). A similar catalytic performance can be obtained using concentrated sunlight as the light source, suggesting the potential prospect of solar-driven DRM. Moreover, the as-prepared catalyst also exhibits superior performance in the dry reforming of ethane and propane. This work paves the way for the rational design of high-performance catalysts for DRM under mild conditions.

ASSOCIATED CONTENT

Ⓢ Supporting Information

The Supporting Information is available free of charge at https://pubs.acs.org/doi/10.1021/jacs.4c02427.

Detailed Experimental Section, characterization methods, and additional material characterizations (PDF)

■ AUTHOR INFORMATION

Corresponding Authors

Ran Long − Hefei National Research Center for Physical Sciences at the Microscale, Key Laboratory of Precision and Intelligent Chemistry, School of Chemistry and Materials Science, National Synchrotron Radiation Laboratory, School of Nuclear Science and Technology, University of Science and Technology of China, Hefei, Anhui 230026, China; orcid.org/0000-0003-4845-9120; Email: longran@ustc.edu.cn

Tingting Kong − Anhui Engineering Research Center of Carbon Neutrality, The Key Laboratory of Functional Molecular Solids, Ministry of Education, Anhui Laboratory of Molecular-Based Materials, College of Chemistry and Materials Science, Anhui Normal University, Wuhu, Anhui 241002, China; Email: 2022045@ahnu.edu.cn

Yujie Xiong − Hefei National Research Center for Physical Sciences at the Microscale, Key Laboratory of Precision and Intelligent Chemistry, School of Chemistry and Materials Science, National Synchrotron Radiation Laboratory, School of Nuclear Science and Technology, University of Science and Technology of China, Hefei, Anhui 230026, China; Suzhou Institute for Advanced Research, University of Science and Technology of China, Suzhou, Jiangsu 215123, China; orcid.org/0000-0002-1995-8257; Email: yjxiong@ustc.edu.cn

Authors

Hailong Xiong − Hefei National Research Center for Physical Sciences at the Microscale, Key Laboratory of Precision and Intelligent Chemistry, School of Chemistry and Materials Science, National Synchrotron Radiation Laboratory, School of Nuclear Science and Technology, University of Science and Technology of China, Hefei, Anhui 230026, China

Yueyue Dong − Hefei National Research Center for Physical Sciences at the Microscale, Key Laboratory of Precision and Intelligent Chemistry, School of Chemistry and Materials Science, National Synchrotron Radiation Laboratory, School of Nuclear Science and Technology, University of Science and Technology of China, Hefei, Anhui 230026, China

Canyu Hu − Hefei National Research Center for Physical Sciences at the Microscale, Key Laboratory of Precision and Intelligent Chemistry, School of Chemistry and Materials Science, National Synchrotron Radiation Laboratory, School of Nuclear Science and Technology, University of Science and Technology of China, Hefei, Anhui 230026, China

Yihong Chen − Hefei National Research Center for Physical Sciences at the Microscale, Key Laboratory of Precision and Intelligent Chemistry, School of Chemistry and Materials Science, National Synchrotron Radiation Laboratory, School of Nuclear Science and Technology, University of Science and Technology of China, Hefei, Anhui 230026, China

Hengjie Liu − Hefei National Research Center for Physical Sciences at the Microscale, Key Laboratory of Precision and Intelligent Chemistry, School of Chemistry and Materials Science, National Synchrotron Radiation Laboratory, School of Nuclear Science and Technology, University of Science and Technology of China, Hefei, Anhui 230026, China; orcid.org/0000-0001-6499-3935

Complete contact information is available at:
https://pubs.acs.org/10.1021/jacs.4c02427

Author Contributions

$^{\parallel}$H.X. and Y.D. contributed equally.

Notes

The authors declare no competing financial interest.

REFERENCES

(1) Li, X.; Wang, C.; Tang, J. Methane transformation by photocatalysis. *Nat. Rev. Mater.* **2022**, 7 (8), 617−632.

(2) Meng, X.; Cui, X.; Rajan, N. P.; Yu, L.; Deng, D.; Bao, X. Direct methane conversion under mild condition by thermo-electro-or photocatalysis. *Chem.* **2019**, 5 (9), 2296−2325.

(3) Li, S.; Gong, J. Strategies for improving the performance and stability of Ni-based catalysts for reforming reactions. *Chem. Soc. Rev.* **2014**, 43 (21), 7245−7256.

(4) Palmer, C.; Upham, D. C.; Smart, S.; Gordon, M. J.; Metiu, H.; McFarland, E. W. Dry reforming of methane catalysed by molten metal alloys. *Nat. Catal.* **2020**, 3 (1), 83−89.

(5) Wu, S.; Li, Y.; Zhang, Q.; Hu, Q.; Wu, J.; Zhou, C.; Zhao, X. Formation of NiCo alloy nanoparticles on Co doped Al_2O_3 leads to high fuel production rate, large light-to-fuel efficiency, and excellent durability for photothermocatalytic CO_2 reduction. *Adv. Energy Mater.* **2020**, 10 (42), 2002602.

(6) Tavasoli, A.; Gouda, A.; Zahringer, T.; Li, Y. F.; Quaid, H.; Viasus Perez, C. J.; Song, R.; Sain, M.; Ozin, G. Enhanced hybrid photocatalytic dry reforming using a phosphated Ni-CeO$_2$ nanorod heterostructure. *Nat. Commun.* **2023**, 14 (1), 1435.

(7) He, C.; Wu, S.; Li, Q.; Li, M.; Li, J.; Wang, L.; Zhang, J. Constructing matched active sites for robust photocatalytic dry reforming of methane. *Chem.* **2023**, 9 (11), 3224−3244.

(8) Zhou, L.; Martirez, J. M. P.; Finzel, J.; Zhang, C.; Swearer, D. F.; Tian, S.; Robatjazi, H.; Lou, M.; Dong, L.; Henderson, L.; Christopher, P.; Carter, E. A.; Nordlander, P.; Halas, N. J. Light-driven methane dry reforming with single atomic site antenna-reactor plasmonic photocatalysts. *Nat. Energy* **2020**, 5 (1), 61−70.

(9) Shoji, S.; Peng, X.; Yamaguchi, A.; Watanabe, R.; Fukuhara, C.; Cho, Y.; Yamamoto, T.; Matsumura, S.; Yu, M. W.; Ishii, S.; Fujita, T.; Abe, H.; Miyauchi, M. Photocatalytic uphill conversion of natural gas beyond the limitation of thermal reaction systems. *Nat. Catal.* **2020**, 3 (2), 148−153.

(10) Shoji, S.; Bin Mohd Najib, A. S.; Yu, M. W.; Yamamoto, T.; Yasuhara, S.; Yamaguchi, A.; Peng, X.; Matsumura, S.; Ishii, S.; Cho, Y.; Fujita, T.; Ueda, S.; Chen, K.-P.; Abe, H.; Miyauchi, M. Charge partitioning by intertwined metal-oxide nano-architectural networks for the photocatalytic dry reforming of methane. *Chem Catal.* **2022**, 2 (2), 321−329.

(11) Zhou, W.; Wang, B. H.; Tang, L.; Chen, L.; Guo, J. K.; Pan, J. B.; Lei, B.; Hu, B.; Bai, Z. J.; Tulu, M.; Li, Z. X.; Wang, X.; Au, C. T.; Yin, S. F. Photocatalytic dry reforming of methane enhanced by "dual-path" strategy with excellent low-temperature catalytic performance. *Adv. Funct. Mater.* **2023**, 33 (27), 2214068.

(12) Zhou, Z.; Li, Y.; Hu, Q.; Wu, J.; Wu, S.; Xie, Z. A novel synergetic effect between Ru and CeO_2 nanoparticles leads to highly efficient photothermocatalytic CO_2 reduction by CH_4 with excellent coking resistance. *Sol. RRL* **2022**, 6 (6), 2101064.

(13) Gao, Y.; Li, Q.; Wang, C.; Yan, D.; Chen, J.; Jia, H. Light-driven efficient dry reforming of methane over Pt/La_2O_3 with long-term durability. *J. Mater. Chem. A* **2022**, 10 (30), 16016−16028.

(14) Han, K.; Wang, Y.; Wang, S.; Liu, Q.; Deng, Z.; Wang, F. Narrowing band gap energy of CeO_2 in $(Ni/CeO_2)@SiO_2$ catalyst for photothermal methane dry reforming. *Chem. Eng. J.* **2021**, 421, 129989.

(15) Yang, Y.; Chai, Z.; Qin, X.; Zhang, Z.; Muhetaer, A.; Wang, C.; Huang, H.; Yang, C.; Ma, D.; Li, Q.; Xu, D. Light-induced redox looping of a Rhodium/Ce_xWO_3 photocatalyst for highly active and robust dry reforming of methane. *Angew. Chem., Int. Ed.* **2022**, 61 (21), No. e202200567.

(16) Wu, S.; Li, Y.; Hu, Q.; Wu, J.; Zhang, Q. Photothermocatalytic dry reforming of methane for efficient CO_2 reduction and solar energy storage. *ACS Sustainable Chem. Eng.* **2021**, 9 (35), 11635−11651.

(17) Xing, F.; Ma, J.; Shimizu, K. I.; Furukawa, S. High-entropy intermetallics on ceria as efficient catalysts for the oxidative dehydrogenation of propane using CO_2. *Nat. Commun.* **2022**, 13 (1), 5065.

(18) Liao, Y.; Li, Y.; Zhao, R.; Zhang, J.; Zhao, L.; Ji, L.; Zhang, Z.; Liu, X.; Qin, G.; Zhang, X. High-entropy-alloy nanoparticles with 21 ultra-mixed elements for efficient photothermal conversion. *Natl. Sci. Rev.* **2022**, 9 (6), nwac041.

(19) Sun, Y.; Dai, S. High-entropy materials for catalysis: A new frontier. *Sci. Adv.* **2021**, 7, No. eabg1600.

(20) Jiang, W.; Loh, H.; Low, B. Q. L.; Zhu, H.; Low, J.; Heng, J. Z. X.; Tang, K. Y.; Li, Z.; Loh, X. J.; Ye, E.; Xiong, Y. Role of oxygen vacancy in metal oxides for photocatalytic CO_2 reduction. *Appl. Catal., B* **2023**, 321, 122079.

(21) Ma, J.; Long, R.; Liu, D.; Low, J.; Xiong, Y. Defect engineering in photocatalytic methane conversion. *Small Struct.* **2021**, 3 (1), 2100147.

(22) Zhao, J.; Guo, X.; Shi, R.; Waterhouse, G. I. N.; Zhang, X.; Dai, Q.; Zhang, T. NiFe nanoalloys derived from layered double hydroxides for photothermal synergistic reforming of CH_4 with CO_2. *Adv. Funct. Mater.* **2022**, 32 (31), 2204056.

(23) Zhang, J.; Wang, L.; Zhao, X.; Shi, L.; Chen, H.; Zhang, S.; Zhang, P.; Wang, S.; Zhang, L. C.; Wang, Y.; Wang, X.; Zhu, Y.; Zhang, H.; Duan, X.; Wu, M.; Shao, G.; Wang, S.; Sun, H. The nature of active sites for plasmon-mediated photothermal catalysis and heat coupled photocatalysis in dry reforming of methane. *Energy Environ. Mater.* **2023**, 6, No. e12416.

(24) Yan, B.; Wu, Q.; Cen, J.; Timoshenko, J.; Frenkel, A. I.; Su, D.; Chen, X.; Parise, J. B.; Stach, E.; Orlov, A.; Chen, J. G. Highly active subnanometer Rh clusters derived from Rh-doped $SrTiO_3$ for CO_2 reduction. *Appl. Catal., B* **2018**, 237, 1003−1011.

(25) Tang, Y.; Li, Y.; Bao, W.; Yan, W.; Zhang, J.; Huang, Y.; Li, H.; Wang, Z.; Liu, M.; Yu, F. Enhanced dry reforming of CO_2 and CH_4 on photothermal catalyst $Ru/SrTiO_3$. *Appl. Catal., B* **2023**, 338, 123054.

(26) Rabuffetti, F.; Kim, H.; Enterkin, J.; Wang, Y.; Lanier, C.; Marks, L.; Poeppelmeier, K.; Stair, P. Synthesis-dependent first-order raman scattering in $SrTiO_3$ nanocubes at room temperature. *Chem. Mater.* **2008**, 20, 5628−5635.

(27) Mori, K.; Hashimoto, N.; Kamiuchi, N.; Yoshida, H.; Kobayashi, H.; Yamashita, H. Hydrogen spillover-driven synthesis of

high-entropy alloy nanoparticles as a robust catalyst for CO_2 hydrogenation. *Nat. Commun.* **2021**, *12* (1), 3884.

(28) Zhu, H.; Sun, S.; Hao, J.; Zhuang, Z.; Zhang, S.; Wang, T.; Kang, Q.; Lu, S.; Wang, X.; Lai, F.; Liu, T.; Gao, G.; Du, M.; Wang, D. A high-entropy atomic environment converts inactive to active sites for electrocatalysis. *Energy Environ. Sci.* **2023**, *16* (2), 619−628.

(29) Liu, Y.; Hsieh, C.; Hsu, L.; Lin, K.; Hsiao, Y.; Chi, C.; Lin, J.; Chang, C.; Lin, S.; Wu, C.; Gao, J.; Pao, C.; Chang, Y.; Lu, M.; Zhou, S.; Yang, T. Toward controllable and predictable synthesis of highentropy alloy nanocrystals. *Sci. Adv.* **2023**, *9*, No. eadf9931.

(30) Horiuchi, T.; Sakuma, K.; Fukui, T.; Kubo, Y.; Osaki, T.; Mori, T. Suppression of carbon deposition in the CO_2-reforming of CH_4 by adding basic metal oxides to a Ni/Al$_2$O$_3$ catalyst. *Appl. Catal., A* **1996**, *144*, 111−120.

(31) Li, Q.; Wang, H.; Zhang, M.; Li, G.; Chen, J.; Jia, H. Suppressive strong metal-support interactions on ruthenium/TiO$_2$ promote light-driven photothermal CO_2 reduction with methane. *Angew. Chem.* **2023**, *135*, No. e202300129.

(32) Li, H.; Hao, C.; Tian, J.; Wang, S.; Zhao, C. Ultra-durable Ni-Ir/MgAl$_2$O$_4$ catalysts for dry reforming of methane enabled by dynamic balance between carbon deposition and elimination. *Chem Catal.* **2022**, *2* (7), 1748−1763.

(33) Xing, F.; Nakaya, Y.; Yasumura, S.; Shimizu, K.-i.; Furukawa, S. Ternary platinum-cobalt-indium nanoalloy on ceria as a highly efficient catalyst for the oxidative dehydrogenation of propane using CO_2. *Nat. Catal.* **2022**, *5* (1), 55−65.

(34) Zhu, M.; Song, Y.; Chen, S.; Li, M.; Zhang, L.; Xiang, W. Chemical looping dry reforming of methane with hydrogen generation on Fe$_2$O$_3$/Al$_2$O$_3$ oxygen carrier. *Chem. Eng. J.* **2019**, *368*, 812−823.

(35) Wang, X.; Pan, W.; Yuan, X.; Li, B. Density-functional theory investigation into the role of Fe doping for improving the carbon resistance over Ni$_3$Fe (111) surface in methane reforming with CO_2. *Appl. Surf. Sci.* **2022**, *574*, 151661.

(36) Hu, Q.; Li, Y.; Wu, J.; Hu, Y.; Cao, H.; Yang, Y. Extraordinary catalytic performance of nickel half-metal clusters for light-driven dry reforming of methane. *Adv. Energy Mater.* **2023**, *13*, 2300071.

(37) Jiang, W.; Low, J.; Mao, K.; Duan, D.; Chen, S.; Liu, W.; Pao, C. W.; Ma, J.; Sang, S.; Shu, C.; Zhan, X.; Qi, Z.; Zhang, H.; Liu, Z.; Wu, X.; Long, R.; Song, L.; Xiong, Y. Pd-Modified ZnO-Au enabling alkoxy intermediates formation and dehydrogenation for photocatalytic conversion of methane to ethylene. *J. Am. Chem. Soc.* **2021**, *143* (1), 269−278.

(38) Zhang, W.; Fu, C.; Low, J.; Duan, D.; Ma, J.; Jiang, W.; Chen, Y.; Liu, H.; Qi, Z.; Long, R.; Yao, Y.; Li, X.; Zhang, H.; Liu, Z.; Yang, J.; Zou, Z.; Xiong, Y. High-performance photocatalytic nonoxidative conversion of methane to ethane and hydrogen by heteroatoms-engineered TiO$_2$. *Nat. Commun.* **2022**, *13* (1), 2806.

(39) Xu, S.; Chansai, S.; Shao, Y.; Xu, S.; Wang, Y. C.; Haigh, S.; Mu, Y.; Jiao, Y.; Stere, C. E.; Chen, H.; Fan, X.; Hardacre, C. Mechanistic study of non-thermal plasma assisted CO_2 hydrogenation over Ru supported on MgAl layered double hydroxide. *Appl. Catal., B* **2020**, *268*, 118752.

(40) Solis-Garcia, A.; Louvier-Hernandez, J. F.; Almendarez-Camarillo, A.; Fierro-Gonzalez, J. C. Participation of surface bicarbonate, formate and methoxy species in the carbon dioxide methanation catalyzed by ZrO$_2$-supported Ni. *Appl. Catal., B* **2017**, *218*, 611−620.

(41) Kattel, S.; Yan, B.; Yang, Y.; Chen, J. G.; Liu, P. Optimizing binding energies of key intermediates for CO_2 hydrogenation to methanol over oxide-supported copper. *J. Am. Chem. Soc.* **2016**, *138* (38), 12440−12450.

(42) Chen, X.; Li, Y.; Pan, X.; Cortie, D.; Huang, X.; Yi, Z. Photocatalytic oxidation of methane over silver decorated zinc oxide nanocatalysts. *Nat. Commun.* **2016**, *7*, 12273.

(43) Yu, X.; De Waele, V.; Lofberg, A.; Ordomsky, V.; Khodakov, A. Y. Selective photocatalytic conversion of methane into carbon monoxide over zinc-heteropolyacid-titania nanocomposites. *Nat. Commun.* **2019**, *10* (1), 700.

(44) Eckle, S.; Anfang, H. G.; Behm, R. J. Reaction intermediates and side products in the methanation of CO and CO_2 over supported Ru catalysts in H$_2$-rich reformate gases. *J. Phys. Chem. C* **2011**, *115*, 1361−1367.

(45) Guo, Y.; Mei, S.; Yuan, K.; Wang, D. J.; Liu, H. C.; Yan, C. H.; Zhang, Y. W. Low-temperature CO_2 methanation over CeO$_2$-supported Ru single atoms, nanoclusters, and nanoparticles competitively tuned by strong metal-support interactions and h-spillover effect. *ACS Catal.* **2018**, *8* (7), 6203−6215.

(46) Wang, X.; Shi, H.; Kwak, J. H.; Szanyi, J. Mechanism of CO_2 hydrogenation on Pd/Al$_2$O$_3$ catalysts: Kinetics and transient DRIFTS-MS studies. *ACS Catal.* **2015**, *5* (11), 6337−6349.

(47) Zhu, J.; Zhang, G.; Li, W.; Zhang, X.; Ding, F.; Song, C.; Guo, X. Deconvolution of the particle size effect on CO_2 hydrogenation over iron-based catalysts. *ACS Catal.* **2020**, *10* (13), 7424−7433.

(48) Galhardo, T. S.; Braga, A. H.; Arpini, B. H.; Szanyi, J.; Goncalves, R. V.; Zornio, B. F.; Miranda, C. R.; Rossi, L. M. Optimizing active sites for high CO selectivity during CO_2 hydrogenation over supported nickel catalysts. *J. Am. Chem. Soc.* **2021**, *143* (11), 4268−4280.

(49) Bobadilla, L. F.; Santos, J. L.; Ivanova, S.; Odriozola, J. A.; Urakawa, A. Unravelling the role of oxygen vacancies in the mechanism of the reverse water-gas shift reaction by operando DRIFTS and ultraviolet-visible spectroscopy. *ACS Catal.* **2018**, *8* (8), 7455−7467.

(50) Zhao, B.; Sun, M.; Chen, F.; Wang, W.; Lu, S.; Zhang, B. Photoinduced reaction pathway change for boosting CO_2 hydrogenation over a MnO-Co catalyst. *ACS Catal.* **2021**, *11* (16), 10316−10323.

(51) Chen, Y.; Zhang, Y.; Fan, G.; Song, L.; Jia, G.; Huang, H.; Ouyang, S.; Ye, J.; Li, Z.; Zou, Z. Cooperative catalysis coupling photo-/photothermal effect to drive Sabatier reaction with unprecedented conversion and selectivity. *Joule* **2021**, *5* (12), 3235−3251.

(52) Kattel, S.; Liu, P.; Chen, J. G. Tuning selectivity of CO_2 hydrogenation reactions at the metal/oxide interface. *J. Am. Chem. Soc.* **2017**, *139* (29), 9739−9754.

(53) Feng, D.; Dong, Y.; Zhang, L.; Ge, X.; Zhang, W.; Dai, S.; Qiao, Z. A. Holey lamellar high-entropy oxide as an ultra-high-activity heterogeneous catalyst for solvent-free aerobic oxidation of benzyl alcohol. *Angew. Chem., Int. Ed.* **2020**, *59* (44), 19503−19509.

(54) Kattel, S.; Yu, W.; Yang, X.; Yan, B.; Huang, Y.; Wan, W.; Liu, P.; Chen, J. G. CO_2 hydrogenation over oxide-supported PtCo catalysts: The role of the oxide support in determining the product selectivity. *Angew. Chem., Int. Ed.* **2016**, *55* (28), 7968−7973.

(55) Mudiyanselage, K.; Senanayake, S. D.; Feria, L.; Kundu, S.; Baber, A. E.; Graciani, J.; Vidal, A. B.; Agnoli, S.; Evans, J.; Chang, R.; Axnanda, S.; Liu, Z.; Sanz, J. F.; Liu, P.; Rodriguez, J. A.; Stacchiola, D. J. Importance of the metal-oxide interface in catalysis: *In situ* studies of the water-gas shift reaction by ambient-pressure X-ray photoelectron spectroscopy. *Angew. Chem. Int. Ed.* **2013**, *52* (19), 5101−5105.

(56) Graciani, J.; Mudiyanselage, K.; Xu, F.; Baber, A.; Evans, J.; Senanayake, S.; Stacchiola, D.; Liu, P.; Hrbek, J.; Sanz, J. F.; Rodriguez, J. A. Highly active copper-ceria and copper-ceria-titania catalysts for methanol synthesis from CO_2. *Science* **2014**, *345*, 546−550.

(57) Li, H.; Rameshan, C.; Bukhtiyarov, A. V.; Prosvirin, I. P.; Bukhtiyarov, V. I.; Rupprechter, G. CO_2 activation on ultrathin ZrO$_2$ film by H$_2$O co-adsorption: *In situ* NAP-XPS and IRAS studies. *Surf. Sci.* **2019**, *679*, 139−146.

(58) Liu, Z. Y.; Huang, E. W.; Orozco, I.; Liao, W. J.; Palomino, R. M.; Rui, N.; Duchon, T.; Nemšák, S.; Grinter, D. C.; Mahapatra, M.; Liu, P.; Rodriguez, J. A.; Senanayake, S. D. Water-promoted interfacial pathways in methane oxidation to methanol on a CeO$_2$-Cu$_2$O catalyst. *Science* **2020**, *368*, 513−517.